

A new method for modelling cohesive cracks using finite elements

G. N. Wells^{1,*},[†] and L. J. Sluys²

¹*Faculty of Aerospace Engineering, Koiter Institute Delft/Delft University of Technology,
P.O. Box 5048, 2600 GA Delft, The Netherlands*

²*Faculty of Civil Engineering and Geosciences, Koiter Institute Delft/Delft University of Technology,
P.O. Box 5048, 2600 GA Delft, The Netherlands*

SUMMARY

A model which allows the introduction of displacements jumps to conventional finite elements is developed. The path of the discontinuity is completely independent of the mesh structure. Unlike so-called ‘embedded discontinuity’ models, which are based on incompatible strain modes, there is no restriction on the type of underlying solid finite element that can be used and displacement jumps are continuous across element boundaries. Using finite element shape functions as partitions of unity, the displacement jump across a crack is represented by extra degrees of freedom at existing nodes. To model fracture in quasi-brittle heterogeneous materials, a cohesive crack model is used. Numerical simulations illustrate the ability of the method to objectively simulate fracture with unstructured meshes. Copyright © 2001 John Wiley & Sons, Ltd.

KEY WORDS: partition of unity; fracture; cohesive crack

1. INTRODUCTION

The computational modelling of propagating discontinuities has long been restricted by the computational tools available. Discontinuities have been limited to inter-element boundaries [1] or the finite element mesh must be changed adaptively to capture a propagating discontinuity [2]. Here a model is developed for modelling propagating cohesive cracks that cross through solid finite elements.

*Correspondence to: G. N. Wells, Faculty of Aerospace Engineering, Koiter Institute Delft/Delft University of Technology, P.O. Box 5048, 2600 GA Delft, The Netherlands

[†]E-mail: g.wells@citg.tudelft.nl

Contract/grant sponsor: STW-Netherlands Technology Foundation

Contract/grant sponsor: Ministry of Economic Affairs, The Netherlands

Contract/grant sponsor: Ministry of Public Works and Water Management, The Netherlands

The challenge in using discontinuous failure models (models with displacement jumps) is to efficiently overcome sensitivity to mesh structure. Obviously, when potential cracks paths are limited to inter-element boundaries the crack path is highly dependent on the mesh structure. The mesh must be aligned *a priori* in order to model a discontinuity. Remeshing techniques, which model a discontinuity by modifying the mesh topology to explicitly capture a discontinuity, are computationally expensive and not readily applicable to non-linear problems [3]. There are, however, significant gains in using discrete failure models. Firstly, discrete models can potentially be used with relatively coarse finite element meshes. This is in contrast with enhanced continuum models for failure [4]. Secondly, discrete models can simply reproduce anisotropy that arises naturally in a cracked medium.

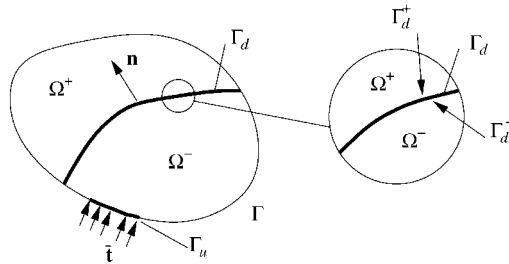
A recent advance in the use of discontinuous models has been the embedment of displacement jumps *within* solid finite elements (so-called embedded discontinuities). In this way, the spatial orientation of a discontinuity is determined by the local stress or strain field, rather than by any pre-defined paths. The displacement jump is incorporated into a finite element as an incompatible mode in the strain field [5–11]. The method is based on enhanced assumed strains (EAS) [12], with the displacement jump represented by an internal element node. For best results, a variationally inconsistent formulation must be used (which results in a non-symmetric stiffness matrix irrespective of the material model used) and following the EAS approach leads to a variational formulation that is based on constant strain elements [11]. However, the formulation has still been applied with other elements.

The formulation developed here is based on partitions of unity [13, 14]. Discontinuous shape functions are used, with the magnitude of the displacement jump represented by extra nodal degrees of freedom at existing nodes. Unlike methods based on EAS, there are no restrictions on allowable element types and displacement jumps are continuous across element boundaries. The displacement jump is added by extending the basis of the underlying finite element interpolation. Functions with displacement jumps are added selectively to the support of individual nodes to model a propagating discontinuity. This method has been used within the element-free Galerkin method [15] and with finite elements [16, 17] to simulate cracks in elastic solids.

In this paper, a fully non-linear model is developed, with tractions as functions of crack opening acting on discontinuity surfaces. The formulation begins by considering the kinematics of a body crossed by a displacement jump. The finite element formulation is developed by considering first the interpolation of the displacement field and then inserting the discontinuous displacement field into the virtual work equation. The cohesive crack concept is used for the simulation of quasi-brittle fracture. To illustrate the excellent performance of the model, numerical examples are shown. The method is shown to be completely independent of the mesh structure and insensitive to the element size. It is also shown that the model succeeds for cases where classical continuum failure models have failed.

2. KINEMATICS OF A DISPLACEMENT JUMP

To incorporate displacement jumps in a finite element interpolation, it is first necessary to examine the kinematic properties of a solid crossed by a discontinuity. Consider the body Ω ($\Omega = \Omega^+ \cup \Omega^-$) shown in Figure 1. The displacement field \mathbf{u} can be decomposed into two

Figure 1. Body Ω crossed by a discontinuity Γ_d .

parts; a continuous and a discontinuous part

$$\mathbf{u}(\mathbf{x}, t) = \hat{\mathbf{u}}(\mathbf{x}, t) + \mathcal{H}_{\Gamma_d} \llbracket \mathbf{u}(\mathbf{x}, t) \rrbracket \quad (1)$$

where $\hat{\mathbf{u}}$ and $\llbracket \mathbf{u} \rrbracket$ are continuous functions on Ω and \mathcal{H}_{Γ_d} is the Heaviside function centred on the discontinuity Γ_d ($\mathcal{H}_{\Gamma_d} = 1$ if $\mathbf{x} \in \Omega^+$, $\mathcal{H}_{\Gamma_d} = 0$ if $\mathbf{x} \in \Omega^-$). The components of the displacement jump at the discontinuity are given by $\llbracket \mathbf{u} \rrbracket_{\mathbf{x} \in \Gamma_d}$.

It is possible to find the strain field for a body crossed by a discontinuity by taking the gradient of Equation (1)

$$\begin{aligned} \boldsymbol{\varepsilon} &= \nabla^s \hat{\mathbf{u}} + \mathcal{H}_{\Gamma_d} (\nabla^s \llbracket \mathbf{u} \rrbracket) + (\nabla \mathcal{H}_{\Gamma_d} \otimes \llbracket \mathbf{u} \rrbracket)^s \\ &= \underbrace{\nabla^s \hat{\mathbf{u}} + \mathcal{H}_{\Gamma_d} (\nabla^s \llbracket \mathbf{u} \rrbracket)}_{\text{bounded}} + \underbrace{\delta_{\Gamma_d} (\llbracket \mathbf{u} \rrbracket \otimes \mathbf{n})^s}_{\text{unbounded}} \end{aligned} \quad (2)$$

where δ_{Γ_d} is the Dirac-delta distribution centred on the discontinuity and \mathbf{n} is the unit normal vector to the discontinuity (pointing to Ω^+). All strains are assumed to be infinitely small, so $(\cdot)^s$ indicates the symmetric part only. Due to the jump in the displacement field, Dirac-delta distributions arise in the strain field. Since the Dirac-delta distribution is unbounded, it is physically meaningless, although it is useful later for inserting the strain field into the virtual work equation.

3. FINITE ELEMENT SHAPE FUNCTIONS AS PARTITIONS OF UNITY

A collection of functions $\varphi_i(\mathbf{x})$, each belonging to a node, defined over a body Ω ($\mathbf{x} \in \Omega$) form a partition of unity if:

$$\sum_{i=1}^n \varphi_i(\mathbf{x}) = 1 \quad (3)$$

where n is the number of nodal points. It has been shown by Duarte and Oden [13] that a field can be interpolated in terms of discrete nodal values using partitions of unity. Using the functions φ_i , an interpolation of u over a body can be formed by

$$u(\mathbf{x}) = \sum_{i=1}^n \varphi_i^k(\mathbf{x}) \left(a_i + \sum_{j=1}^m b_{ij} \gamma_j(\mathbf{x}) \right) \quad (4)$$

where φ_i^k are partition of unity functions of order k (if the partition of unity functions are polynomials, k refers to the polynomial order), a_i are ‘regular’ nodal degrees of freedom, b_{ij} are ‘enhanced’ nodal degrees of freedom and γ_j is an ‘enhanced’ basis with m terms. To avoid linear dependency, the order of any polynomial terms in the enhanced basis must be greater than k .

It is Equation (4) that provides the link between meshless methods and the finite element method. The differences between the methods lies in the choice of the functions $\varphi_i(\mathbf{x})$. The element-free Galerkin method [18] uses a weighted moving least-squares function of order k with, in general, an empty enhanced basis as the partition of unity. More generally, *hp* clouds [13] use a weighted moving least-squares function of order k (which can be of order zero) with a non-empty enhanced basis. Importantly, finite element shape functions are also partitions of unity, since

$$\sum_{i=1}^n N_i(\mathbf{x}) = 1 \quad (5)$$

where N_i are finite element shape functions. The difference between the finite element method and meshless methods lies solely in the choice of the partition of unity functions. In the conventional form of the finite element method, the order of the partition of unity function is the polynomial order of the shape functions and the enhanced basis is empty. There is however no reason why the enhanced basis cannot be used with finite elements. In finite element notation, the interpolation of the displacement field, using the partition of unity property, can be written as

$$\mathbf{u}(\mathbf{x}) = \underbrace{\mathbf{N}(\mathbf{x})\mathbf{a}}_{\text{standard}} + \underbrace{\mathbf{N}(\mathbf{x})(\mathbf{N}_\gamma(\mathbf{x})\mathbf{b})}_{\text{enhanced}} \quad (6)$$

where \mathbf{N} is a matrix containing the usual (polynomial) shape functions of polynomial order k , \mathbf{a} contains the regular nodal degrees of freedom, \mathbf{N}_γ is a matrix containing the enhanced basis terms and \mathbf{b} contains the enhanced nodal degrees of freedom. The number of enhanced degrees of freedom per node is equal to the number of terms in the enhanced basis multiplied by the spatial dimension. The vector form of the strain field in terms of nodal displacements can be written as

$$\boldsymbol{\varepsilon} = \nabla^s \mathbf{u} = \mathbf{B}\mathbf{a} + \mathbf{B}_\gamma \mathbf{b} \quad (7)$$

where $\mathbf{B} = \mathbf{L}\mathbf{N}$ and $\mathbf{B}_\gamma = \mathbf{L}(\mathbf{N}\mathbf{N}_\gamma)$. The matrix \mathbf{L} contains differential operators:

$$\mathbf{L} = \begin{bmatrix} \frac{\partial}{\partial x} & 0 & 0 \\ 0 & \frac{\partial}{\partial y} & 0 \\ 0 & 0 & \frac{\partial}{\partial z} \\ \frac{\partial}{\partial y} & \frac{\partial}{\partial x} & 0 \\ 0 & \frac{\partial}{\partial z} & \frac{\partial}{\partial y} \\ \frac{\partial}{\partial z} & 0 & \frac{\partial}{\partial x} \end{bmatrix} \quad (8)$$

The enhanced basis can be used to improve the interpolation of the displacement field. It can be used to facilitate a form of p -adaptivity [19] or to add analytical information to the solution [16, 17]. The critical feature of the interpolation in Equation (6) is that the interpolation is constructed on a per-node basis. It is possible to enhance individual nodes to improve a solution without modifying the original finite element mesh.

3.1. Inclusion of discontinuities in the enhanced basis

In order to model discontinuities in the displacement field, it is possible to add discontinuous functions to the enhanced basis. Examining the displacement decomposition in Equation (1), it can be seen that it is similar in form to the displacement interpolation in Equation (6). The matrix \mathbf{N} together with the regular degrees of freedom \mathbf{a} can be considered to represent the continuous part $\hat{\mathbf{u}}$ and the matrix product $\mathbf{N}\mathbf{N}_\gamma$ together with the enhanced degrees of freedom \mathbf{b} represent the discontinuous part $\mathcal{H}_{\Gamma_d}[\![\mathbf{u}]\!]$. Further, for the discontinuous part, the continuous function $[\![\mathbf{u}]\!]$ is interpolated by \mathbf{N} and the Heaviside jump \mathcal{H}_{Γ_d} is contained within \mathbf{N}_γ . Inserting the Heaviside function into the enhanced basis for Equation (6), the displacement field in elements where the extra degrees of freedom are active can be written as

$$\mathbf{u}(\mathbf{x}) = \underbrace{\mathbf{N}(\mathbf{x})\mathbf{a}}_{\hat{\mathbf{u}}} + \mathcal{H}_{\Gamma_d} \underbrace{\mathbf{N}(\mathbf{x})\mathbf{b}}_{[\![\mathbf{u}]\!]}. \quad (9)$$

Accordingly, the strain field in elements where the enhanced degrees of freedom are active can be expressed as

$$\boldsymbol{\varepsilon} = \mathbf{B}\mathbf{a} + \mathcal{H}_{\Gamma_d}\mathbf{B}\mathbf{b} + (\delta_{\Gamma_d}\mathbf{n})\mathbf{N}\mathbf{b} \quad (10)$$

where \mathbf{n} contains the normal components to the discontinuity. In matrix notation,

$$\mathbf{n}^T = \begin{bmatrix} n_x & 0 & 0 & n_y & 0 & n_z \\ 0 & n_y & 0 & n_x & n_z & 0 \\ 0 & 0 & n_z & 0 & n_y & n_x \end{bmatrix} \quad (11)$$

Effectively, the regular degrees of freedom \mathbf{a} represent the continuum part, while the enhanced degrees of freedom \mathbf{b} represent the displacement jump across the discontinuity. Adding

the Heaviside function \mathcal{H} to the enhanced basis for finite elements results in a displacement jump along a discontinuity of the same order as the interpolating polynomial shape functions.

4. VARIATIONAL FORMULATION

The virtual work equation without body forces reads:

$$\int_{\Omega} \nabla^s \boldsymbol{\eta} : \boldsymbol{\sigma} \, d\Omega = \int_{\Gamma_u} \boldsymbol{\eta} \cdot \bar{\mathbf{t}} \, d\Gamma \quad (12)$$

where $\boldsymbol{\eta}$ are admissible displacement variations, $\boldsymbol{\sigma}$ is the stress field and $\bar{\mathbf{t}}$ are external traction forces, applied on the boundary Γ_u . Inserting the strain field from Equation (2) into the virtual work equation results in

$$\int_{\Omega} \nabla^s \hat{\boldsymbol{\eta}} : \boldsymbol{\sigma} \, d\Omega + \int_{\Omega} \mathcal{H}_{\Gamma_d}(\nabla^s \llbracket \boldsymbol{\eta} \rrbracket) : \boldsymbol{\sigma} \, d\Omega + \int_{\Omega} \delta_{\Gamma_d}(\llbracket \boldsymbol{\eta} \rrbracket \otimes \mathbf{n})^s : \boldsymbol{\sigma} \, d\Omega = \int_{\Gamma_u} \hat{\boldsymbol{\eta}} \cdot \bar{\mathbf{t}} \, d\Gamma \quad (13)$$

A condition on the enhanced part of the displacement field $\llbracket \mathbf{u} \rrbracket$, imposed for practical reasons, is that it be zero where natural and essential boundary conditions are imposed. This condition simplifies the method and avoids the need for complex procedures in order to apply essential boundary conditions and avoids the appearance of $\llbracket \boldsymbol{\eta} \rrbracket$ on the RHS of Equation (13). Integrating the Dirac-delta distribution in Equation (13) over the body Ω , the unbounded term disappears,

$$\int_{\Omega} \nabla^s \hat{\boldsymbol{\eta}} : \boldsymbol{\sigma} \, d\Omega + \int_{\Omega} \mathcal{H}_{\Gamma_d}(\nabla^s \llbracket \boldsymbol{\eta} \rrbracket) : \boldsymbol{\sigma} \, d\Omega + \int_{\Gamma_d} \llbracket \boldsymbol{\eta} \rrbracket_{\Gamma_d} \cdot \mathbf{t} \, d\Gamma = \int_{\Gamma_u} \hat{\boldsymbol{\eta}} \cdot \bar{\mathbf{t}} \, d\Gamma \quad (14)$$

where $\mathbf{t} (= (\boldsymbol{\sigma} \mathbf{n})_{\Gamma_d})$ are the traction forces acting on the discontinuity.

Taking variations $\llbracket \boldsymbol{\eta} \rrbracket$ ($\hat{\boldsymbol{\eta}} = \mathbf{0}$), it follows from Equation (14) that the Heaviside jump can be eliminated by integrating only over Ω^+ .

$$\int_{\Omega^+} (\nabla^s \llbracket \boldsymbol{\eta} \rrbracket) : \boldsymbol{\sigma} \, d\Omega + \int_{\Gamma_d} \llbracket \boldsymbol{\eta} \rrbracket_{\Gamma_d} \cdot \mathbf{t} \, d\Gamma = 0 \quad (15)$$

The above equation ensures that traction continuity is satisfied in a weak sense. Defining Γ_d^+ and Γ_d^- as the surface Γ_d from the Ω^+ and Ω^- sides, respectively (see Figure 1), from the displacement decomposition in Equation (1), the contribution of $\llbracket \boldsymbol{\eta} \rrbracket$ is always zero on Γ_d^- and can be non-zero on Γ_d^+ . The consequence is that the traction forces at the discontinuity are ‘acting’ on Γ_d^+ and are resisted by an equivalent force in the continuum body Ω^+ .

4.1. Discretised equations

To form the stiffness matrix and internal force vector, the discretised interpolations are inserted into the virtual work equation. From Equation (9), variations $\hat{\boldsymbol{\eta}}$ and $\llbracket \boldsymbol{\eta} \rrbracket$ in terms of variations of nodal displacements are written as

$$\hat{\boldsymbol{\eta}} = \mathbf{N} \mathbf{a}' \quad (16a)$$

$$\llbracket \boldsymbol{\eta} \rrbracket = \mathbf{N} \mathbf{b}' \quad (16b)$$

where \mathbf{a}' and \mathbf{b}' are variations of the nodal degrees of freedom \mathbf{a} and \mathbf{b} , respectively. The gradient of the variations $\hat{\boldsymbol{\eta}}$ and $\llbracket \boldsymbol{\eta} \rrbracket$ can be written in a discretised form as

$$\nabla^s \hat{\boldsymbol{\eta}} = \mathbf{L} \mathbf{N} \mathbf{a}' = \mathbf{B} \mathbf{a}' \quad (17a)$$

$$\nabla^s \llbracket \boldsymbol{\eta} \rrbracket = \mathbf{L} \mathbf{N} \mathbf{b}' = \mathbf{B} \mathbf{b}' \quad (17b)$$

Inserting the discretised form of displacement variations into Equation (14) and taking first variations $\hat{\boldsymbol{\eta}}$ and then of $\llbracket \boldsymbol{\eta} \rrbracket$ yields

$$\int_{\Omega} \mathbf{B}^T \boldsymbol{\sigma} d\Omega = \int_{\Gamma_u} \mathbf{N}^T \bar{\mathbf{t}} d\Gamma \quad (18a)$$

$$\int_{\Omega^*} \mathcal{H}_{\Gamma_d} \mathbf{B}^T \boldsymbol{\sigma} d\Omega + \int_{\Gamma_d} \mathbf{N}^T \mathbf{t} d\Gamma = \mathbf{0} \quad (18b)$$

Note that the integration domain of the first integral in Equation (18b) is Ω^* , which indicates the parts of the body Ω where $\llbracket \boldsymbol{\eta} \rrbracket$ is non-zero. From Equation (18), the equivalent nodal forces corresponding to variations of the regular degrees of freedom \mathbf{a} and to the enhanced degrees of freedom \mathbf{b} are written as

$$\mathbf{f}_a^{\text{int}} = \int_{\Omega} \mathbf{B}^T \boldsymbol{\sigma} d\Omega \quad (19a)$$

$$\mathbf{f}_b^{\text{int}} = \int_{\Omega^*} \mathcal{H}_{\Gamma_d} \mathbf{B}^T \boldsymbol{\sigma} d\Omega + \int_{\Gamma_d} \mathbf{N}^T \mathbf{t} d\Gamma \quad (19b)$$

where subscripts 'a' and 'b' have been added to denote variations of the regular and enhanced parts, respectively. The internal force vector $\mathbf{f}_a^{\text{int}}$ in Equation (19a) is of the usual form for finite elements, and the internal force vector $\mathbf{f}_b^{\text{int}}$ in Equation (19b) must be zero (from Equation (15)), imposing traction continuity in a weak sense. To develop an efficient incremental solution procedure, the constitutive relations must be posed in a rate form. The stress rate in the bulk of the continuum can be expressed in terms of nodal displacement velocities as

$$\dot{\boldsymbol{\sigma}} = \mathbf{D} \dot{\boldsymbol{\varepsilon}} = \mathbf{D}(\mathbf{B} \dot{\mathbf{a}} + \mathcal{H}_{\Gamma_d} \mathbf{B} \dot{\mathbf{b}}) \quad (20)$$

where \mathbf{D} relates the instantaneous stress and strain rates. Similarly, the traction rate at the discontinuity can be expressed in terms of the enhanced nodal velocities as

$$\dot{\mathbf{t}} = \mathbf{T} \llbracket \dot{\mathbf{u}} \rrbracket = \mathbf{T} \mathbf{N} \dot{\mathbf{b}} \quad (21)$$

where \mathbf{T} relates the instantaneous traction and crack displacement rates. Substitution of the stress and traction rates into the discretised form of the virtual work Equation (18) leads to the stiffness matrix \mathbf{K} in terms of incremental displacements ($d\mathbf{a}, d\mathbf{b}$),

$$\underbrace{\begin{bmatrix} \int_{\Omega} \mathbf{B}^T \mathbf{D} \mathbf{B} d\Omega & \int_{\Omega^*} \mathcal{H}_{\Gamma_d} \mathbf{B}^T \mathbf{D} \mathbf{B} d\Omega \\ \int_{\Omega^*} \mathcal{H}_{\Gamma_d} \mathbf{B}^T \mathbf{D} \mathbf{B} d\Omega & \int_{\Omega^*} \mathcal{H}_{\Gamma_d} \mathbf{B}^T \mathbf{D} \mathbf{B} d\Omega + \int_{\Gamma_d} \mathbf{N}^T \mathbf{T} \mathbf{N} d\Gamma \end{bmatrix}}_{\mathbf{K}} \begin{Bmatrix} d\mathbf{a} \\ d\mathbf{b} \end{Bmatrix} = \begin{Bmatrix} \mathbf{f}^{\text{ext}} \\ \mathbf{0} \end{Bmatrix} - \begin{Bmatrix} \mathbf{f}_a^{\text{int}} \\ \mathbf{f}_b^{\text{int}} \end{Bmatrix} \quad (22)$$

where \mathbf{f}^{ext} are the externally applied forces (see RHS of Equation (18a)).

5. DISCRETE CONSTITUTIVE MODEL

The discrete constitutive model applied (in terms of tractions and displacements) is based on the cohesive crack concept [21], in which all inelastic deformation around a crack tip is compressed onto a line and represented as traction forces acting on a crack, or acting on a fictional extension of a crack. The constitutive model is formed in an orthogonal local n, s coordinate system, with the n direction normal to the discontinuity. Away from the discontinuity, elastic behaviour is assumed in the bulk of the material. Therefore, the material tangent \mathbf{D} in Equation (20) is the elastic constitutive tangent.

5.1. Traction–separation relationship

The model applied here has been used successfully for the three-dimensional simulation of fracture in concrete using the EAS-based embedded discontinuity model [11]. In this section, the constitutive formulation is limited to two dimensions. A loading function f is defined as

$$f(\llbracket u \rrbracket_n, \kappa) = \llbracket u \rrbracket_n - \kappa \quad (23)$$

where $\llbracket u \rrbracket_n$ is the normal separation at the interface (positive displacement indicates crack opening) and κ is a history parameter, equal to the largest value of $\llbracket u \rrbracket_n$ reached. Loading (opening) at a discontinuity is indicated by $f \geq 0$ and unloading by $f < 0$.

The normal traction force t_n transmitted across a discontinuity is made an exponentially decaying function of the history parameter

$$t_n = f_t \exp\left(-\frac{f_t}{G_f} \kappa\right) \quad (24)$$

where f_t is the tensile strength of the material and G_f is the fracture energy. The crack shear stiffness is also made a function of the history parameter. The shear traction t_s acting on the discontinuity surface is calculated from

$$t_s = d_{\text{int}} \exp(h_s \kappa) \llbracket u \rrbracket_s \quad (25)$$

where d_{int} is the initial crack shear stiffness (when $\kappa = 0$), $\llbracket u \rrbracket_s$ is the crack sliding displacement and h_s is equal to:

$$h_s = \ln(d_{\kappa=1.0}/d_{\text{int}}) \quad (26)$$

where $d_{\kappa=1.0}$ is the crack shear stiffness when $\kappa = 1.0$. Softening behaviour at the interface is driven only by normal separation at the interface, although as the interface opens, the crack shear stiffness approaches zero.

The preceding relationships for the tractions forces on a discontinuity in terms of crack displacements can be differentiated with respect to time to form a consistently linearized tangent.

$$\begin{Bmatrix} \dot{i}_n \\ \dot{i}_s \end{Bmatrix} = \underbrace{\begin{bmatrix} -\frac{f_t^2}{G_f} \exp\left(-\frac{f_t}{G_f} \kappa\right) & 0 \\ h_s d_{\text{int}} \exp(h_s \kappa) \llbracket u \rrbracket_s & d_{\text{int}} \exp(h_s \kappa) \end{bmatrix}}_{\mathbf{T}} \begin{Bmatrix} \llbracket \dot{u} \rrbracket_n \\ \llbracket \dot{u} \rrbracket_s \end{Bmatrix} \quad (27)$$

Note that the dependence of the shear stiffness on the normal separation results in a non-symmetric tangent. A simplification of the above model, with significant computational advantages, is to make the crack shear stiffness constant. The benefit is that the material tangent \mathbf{T} becomes symmetric, hence the global stiffness matrix is also symmetric. The danger of a constant shear stiffness is that if it is made too small, an overly brittle post-peak global response is predicted, and if the shear stiffness is too high, stress locking is observed [22].

Unloading behaviour is simulated using the secant stiffness. Upon full crack closure ($\llbracket u \rrbracket_n = 0$), elastic stiffness recovery is assumed.

6. NUMERICAL IMPLEMENTATION

The numerical procedure is implemented using the six-noded triangle as the underlying finite element and plane strain conditions are assumed. During a calculation, the principal tensile stresses are checked at all integration points in the element ahead of a discontinuity tip at the end of a load increment. If the maximum principal tensile stress at any of the integration points in the element ahead of the crack exceeds the tensile strength of the material, a discontinuity is introduced through the entire element. Discontinuities are introduced as straight lines within elements (the normal vector to the discontinuity \mathbf{n} is constant within an element). Since within the cohesive crack framework energy is dissipated upon crack opening rather than upon crack extension (as with linear elastic fracture), the numerical result is not particularly sensitive to exactly when a discontinuity is extended or the length of the discontinuity extension. It is possible (and is inevitable upon mesh refinement) that a discontinuity propagates through more than one element at the end of a load increment. The introduction of a discontinuity through an entire element can lead to stress jumps upon introduction of a discontinuity, although experience indicates that this has no influence on the robustness of the algorithm, and upon mesh refinement the stress jump approaches zero.

Unlike continuum-type models, in this model a crack must propagate from a discrete point. Therefore, discontinuities can be initiated in two ways, the first being by choosing a point before the calculation and the second by performing an elastic loading step and checking where the principal stresses are greatest. In this way, the method is more closely related to linear-elastic fracture simulations where a crack must propagate from a point. Discontinuities are extended only at the end of a load increment in order to preserve the quadratic convergence rate of the full Newton–Raphson solution procedure. The method is efficient since quadratic convergence can be achieved (typically two to three iterations are required per load increment), even with large load increments.

6.1. Determination of the normal vector

The most important consideration when extending a discontinuity is that the correct direction is chosen. Since the tip of a discontinuity is not located at a point where the stresses are known accurately (such as conventional Gauss points), the local stress field cannot be relied upon to accurately yield the correct normal vector to a discontinuity. To overcome this, non-local stresses at the discontinuity tip are calculated and used to find the principal directions. The non-local stress tensor is calculated as a weighted average of stresses using a Gaussian

weight function

$$w = \frac{1}{(2\pi)^{3/2} l^3} \exp\left(-\frac{r^2}{2l^2}\right) \quad (28)$$

where w is the weight, l determines how quickly the weight function decays away from the discontinuity tip and r is the distance of a point from a crack tip. It is emphasized that this does not imply any non-locality in the model, but is a method of smoothing stresses in order to accurately determine the principal stress directions. The parameter l is taken as approximately three times the typical element size. It is noted that Jirasek [23] found that using a non-local measure for determining the direction of discontinuity propagation with an EAS-based model lead to a more reliable prediction of the crack path.

6.2. Enhancement of individual nodes

In the previous sections, no mention has been made of which nodes are enhanced by displacement jumps. Since the functions in the enhanced basis γ are multiplied by the shape functions of a particular node, the enhanced basis at a particular node has an influence only over the support of that node. Therefore, the Heaviside function is added only to the enhanced basis of nodes whose support is crossed by a discontinuity.

Another condition that must be satisfied is that the displacement jump at the crack tip be zero. To ensure this, the nodes on the element boundary *touched* by a discontinuity tip are not enhanced. When a discontinuity propagates into the next element, all nodes behind the crack tip are enhanced. This is illustrated in Figure 2.

6.3. Integration scheme

When using non-standard shape functions, the question arises how the numerical integration should be performed. The most important requirement when using discontinuous functions is that the strain field is adequately integrated on both sides of the discontinuity. Failure to integrate on both sides of a discontinuity results in a linearly dependent system of equations since the Heaviside function cannot be distinguished from a constant function. Often when a discontinuity crosses an element, the initial Gauss integration scheme is not sufficient to ensure that the shape functions remain linearly independent.

Elements which are not crossed by a discontinuity are integrated by standard three-point Gauss quadrature. When an element is first crossed by a discontinuity, the domains Ω_e^+ and Ω_e^- on either side of the discontinuity are triangulated into sub-domains. Within each triangular sub-domain, three-point Gauss quadrature is applied. In addition to integration points in the bulk of the element, two integration points are positioned on the discontinuity in order to integrate the traction forces. The integration scheme is illustrated in Figure 3. The proposed integration scheme requires 23 integration points per element which at first seems excessive. However, since only elements crossed by a discontinuity require the modified integration scheme, the computational burden is small. In the bulk of the element, the proposed scheme over-integrates the stress field. The scheme is adopted for maximum flexibility since it may be desirable to add enhancement functions other than the Heaviside jump (for example, the near-tip fields for linear-elastic fracture mechanics [16]). It is undesirable that the integration scheme be modified for every different set of enhancement functions since the computational cost of over integrating a small number of elements is negligible.

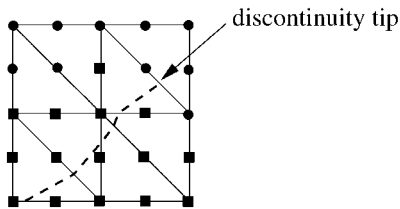


Figure 2. Enhanced nodes whose support is crossed by a discontinuity (dashed line). Enhanced nodes are indicated by the squares and regular nodes by the circles.

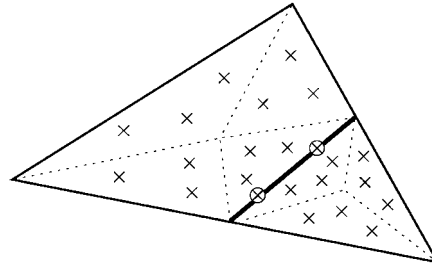


Figure 3. Integration scheme for a six-noded triangular element crossed by a discontinuity (heavy line). The crosses are integration points for the continuum and the crosses inside a circle are integration points for the traction forces on the discontinuity.

7. NUMERICAL EXAMPLES

For practical application, of prime interest is whether the proposed model is independent of the spatial discretisation. The numerical examples test the method for objectivity with respect to element size and mesh alignment. To do this, both the global response (load–displacement) and the local response (crack path) are carefully examined for two different problems. For all numerical examples in this section, only one crack is allowed to propagate. In principle, there is no limitation to the number of cracks that can be simulated. For the case where cracks interact (two or more discontinuities within the support of a node), extra nodal degrees of freedom are required for each crack, plus degrees of freedom that represent the interaction between cracks.

7.1. Three-point bending test

A simply supported beam is loaded symmetrically by means of an imposed displacement at the centre of the beam on the top edge (Figure 4). The following material properties are used: Young's modulus $E = 100$ MPa, Poisson's ratio $\nu = 0.0$, tensile strength $f_t = 1.0$ MPa and fracture energy $G_f = 0.1$ N/mm. For this example, the crack shear stiffness is set to zero, making the discrete material tangent \mathbf{T} symmetric. Since the crack shear stiffness is zero, the top row of elements of the beam are prevented from cracking since if a crack propagates through the entire beam, the system of equations becomes singular as the beam has no shear resistance and rigid body modes are not restrained.

Figure 5 shows the crack through the beam for two meshes, one with 523 elements and the other with 850 elements. A crack is initiated at the centre of the beam. It can be seen that for both meshes a crack propagates directly upwards towards the load point. The crack is able to propagate independently of any mesh alignment. Figure 6 shows the mesh with 523 elements with a crack forced to initiate eccentrically. Offsetting the crack slightly ($x = 5.7$, 0.7 mm offset) tests the ability of the method to model a curved crack. It can be seen in that the crack curves towards the centre of the beam, crossing the directional bias of the mesh.

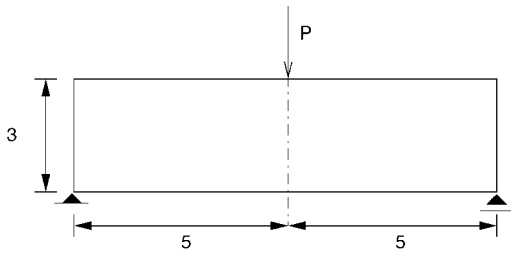


Figure 4. Three-point bending beam. All dimensions in millimetres (depth = 1 mm).

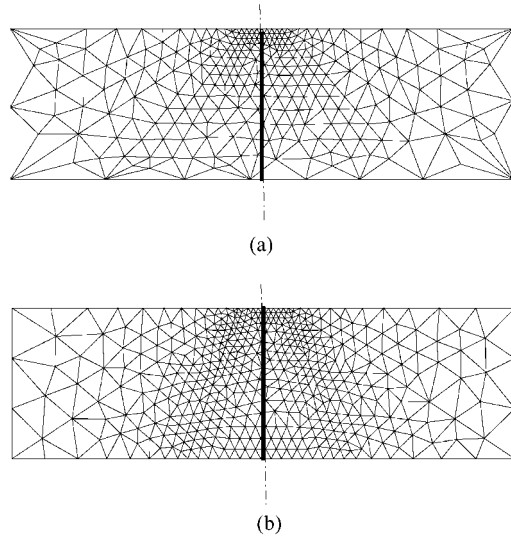


Figure 5. Crack paths for three-point bending test with: (a) 523 elements; and (b) 850 elements. Cracks are shown by the heavy lines.

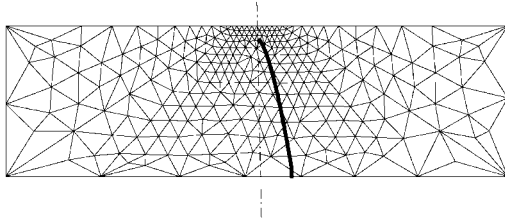


Figure 6. Crack path for mesh with 523 elements and eccentric crack (0.7 mm offset). The crack is shown by the heavy line.

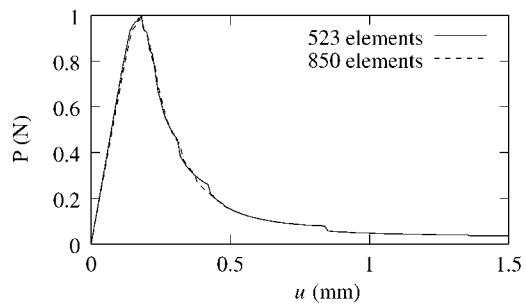


Figure 7. Load-displacement response for three-point bending test.

The load-displacement response of the three-point bending test with the concentric crack is shown in Figure 7. Integrating the load-displacement response for the mesh with 523 elements shows that the energy dissipated is equal to 0.3080 Nmm. This agrees well with the fracture energy multiplied by the depth of the beam which equals 0.3 Nmm, indicating that the energy dissipated is independent of the spatial discretisation. The small difference in the calculated and input fracture energy is due to the top row of elements being prevented from cracking.

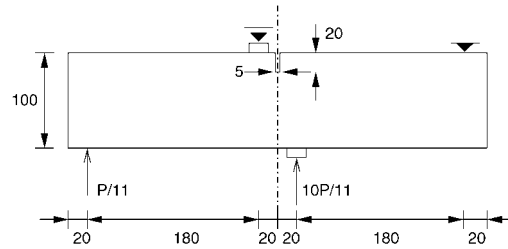


Figure 8. SEN beam. All dimensions in millimetres (depth = 100 mm).

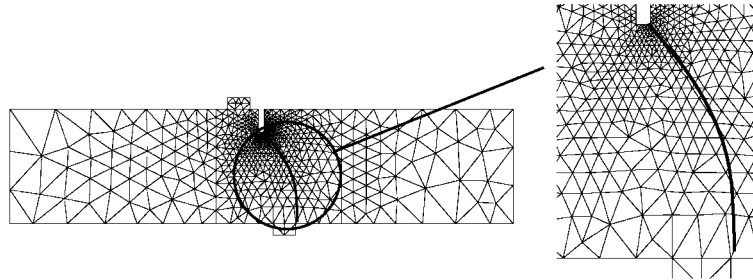


Figure 9. SEN beam with 1184 elements. The crack is shown by the heavy line.

7.2. Single-edge notched (SEN) beam

A more challenging example is the SEN beam (Figure 8). Experimentally, it has been observed that a curved crack propagates from the notch towards the RHS of the central load point [24]. Previous attempts to model the SEN beam with continuum models based on principal stress or strain criteria have yielded reasonable load–displacement responses, but have failed to capture the curved crack. Generally, with continuum models a straight crack propagates from the notch directly downwards. To model the curved crack with a continuum damage model, Peerlings *et al.* [25] used a modified Von Mises criteria for damage growth. Similarly, it was shown for EAS-based embedded discontinuity models that a pure principal stress criterion for the introduction of a discontinuity results in a crack that propagates directly downwards [11] and that a modified Von Mises criteria was required to simulate a curved crack. For the analysis of the SEN beam, the following materials properties are used: Young's modulus $E = 3.5 \times 10^4$ MPa, Poisson's ratio $\nu = 0.2$, tensile strength $f_t = 3.0$ MPa and fracture energy $G_f = 0.1$ N/mm. The material parameters have been taken from Schlangen [24]. At the central loading point and the support near the notch, the loading plates have the material properties of steel. The calculation is performed under load control using an arc-length solution procedure. The relative difference in vertical displacements on each side of the notch (crack mouth sliding displacement, cmsd) is used to control the solution procedure.

It can be seen in Figure 9 that the predicted crack path is curved. This is in excellent agreement with experimental results [24]. Examining the crack path closely, it can be seen that the crack path is independent of the mesh structure. It is emphasized that the curved crack path is computed using a principal stress initiation criterion. To further examine the

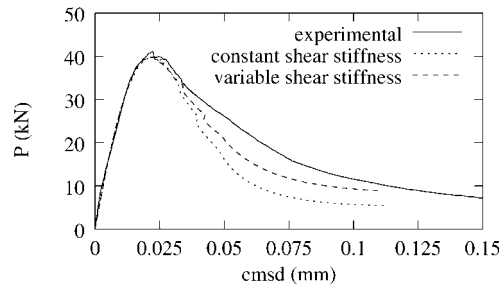


Figure 10. Applied load plotted against crack mouth sliding displacement (cmsd) for experimental results [24] and simulations with variable shear stiffness ($d_{\text{init}} = 1.0 \times 10^2 \text{ N/mm}$, $d_{\kappa=1.0} = 1.0 \times 10^{-4} \text{ N/mm}$) and constant shear stiffness ($d_{\text{init}} = 1.0 \text{ N/mm}$).

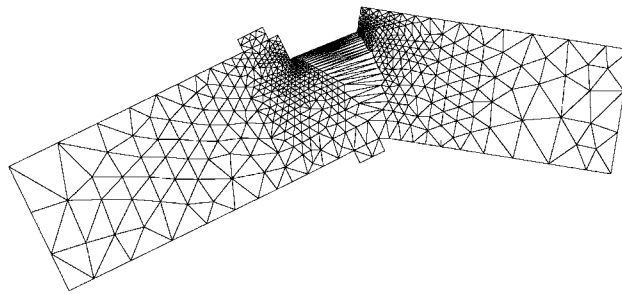


Figure 11. Deformed mesh for the SEN beam with 1184 elements.

numerical results, the load–displacement response of the simulation is compared to the experimental results in Figure 10. It can be seen that the calculated peak load is very close to the experimentally measured peak load. The post-peak response is also close to the experimental results. Matching the experimental post-peak response requires some fitting of the material parameters, particularly the shear stiffness. The crack shear stiffness has almost no influence on the peak strength, but has a significant influence on the ductility of the post-peak response. The deformed mesh is shown in Figure 11.

8. CONCLUSIONS

A new method for modelling cohesive cracks has been presented. The model is based on using finite element shape functions as partitions of unity. The underlying polynomial basis is enhanced with the discontinuous Heaviside jump function in the displacement field. This allows displacement discontinuities within solid finite elements. For the modelling of quasi-brittle materials, a cohesive crack model is used. Numerical examples show that a discontinuity can propagate through an unstructured finite element mesh independently of the mesh structure and the result is insensitive to the finite element size. It is also shown that it is possible to model a curved crack, which has proved difficult with other models. For all examples, excellent results are achieved with relatively coarse finite element meshes. It is, however, essential that

a fine mesh be used in regions where stress gradients are high in order to accurately calculate the normal vector to the discontinuity path.

The partition of unity idea for interpolating fields comes from so-called ‘meshless methods’. The use here of finite element shape functions as partitions of unity provides much of the flexibility of meshless methods with the computational efficiency and robustness of finite elements. The method can be implemented in existing finite element codes by allocating extra degrees of freedom at all nodes and restraining the unused degrees of freedom or eliminating the unused degrees of freedom from the global stiffness matrix. The model offers several advantages over EAS-based embedded discontinuity models. Namely,

- the method is variationally consistent (which is not the case for all EAS-based approaches);
- displacement jumps are continuous across element boundaries and the interpolation of the jump can be of any polynomial order;
- if the material tangent is symmetric, symmetry of the global stiffness matrix is preserved; and
- the method can be implemented with any underlying base element.

When compared to EAS-based models, the advantages come at the cost of increased complexity in implementation since extra global degrees of freedom are required during a calculation and the integration scheme must be adapted in some elements. However, these aspects can be incorporated in a highly automated manner.

The procedure has the potential to be computationally efficient since only a relatively small number of the total number of nodes need be enhanced, it performs robustly with large load increments and convergence of the Newton–Raphson scheme is quadratic. The potential efficiency makes the method well-suited for large-scale analyses. A crucial advantage over conventional interface elements is that deformations at the discontinuity are purely inelastic. The consequence is that there is no need for a ‘dummy’ elastic stiffness which enhances the robustness of the numerical procedure. An essential requirement for efficient implementation is a flexible finite element code which allows the number of degrees of freedom per node and the number of integration points per element to be varied during a calculation. The ease with which the underlying finite element basis can be enhanced makes this a promising procedure for simulating failure and other highly localized phenomena.

ACKNOWLEDGEMENTS

This research is supported by the Technology Foundation STW, applied science division of NWO and the technology program of the Ministry of Economic Affairs and the Ministry of Public Works and Water Management, The Netherlands.

REFERENCES

1. Schellekens JCJ, De Borst R. On the numerical integration of interface elements. *International Journal for Numerical Methods in Engineering* 1993; **26**(1):43–66.
2. Swenson DV, Ingraffea AR. Modeling mixed-mode dynamic crack propagation using finite elements: Theory and applications. *Computational Mechanics* 1988; **3**(5):381–397.
3. Bittencourt TN, Ingraffea AR, Llorca J. Simulation of arbitrary, cohesive crack propagation. In *Fracture Mechanics of Concrete Structures*, Bazant ZP (ed.). Elsevier: London, 1992; 339–350.

4. De Borst R, Sluys LJ, Mülhaus HB, Pamin J. Fundamental issues in finite element analyses of localization and deformation. *Engineering Computations* 1993; **10**(5):99–121.
5. Dvorkin EN, Cuitiño AM, Gioia G. Finite-elements with displacement interpolated embedded localization lines insensitive to mesh size and distortions. *International Journal for Numerical Methods in Engineering* 1990; **30**(3):541–564.
6. Klisinski M, Runesson K, Sture S. Finite element with inner softening band. *ASCE Journal of Engineering Mechanics* 1991; **117**(3):575–587.
7. Simo JC, Oliver J, Armero F. An analysis of strong discontinuities induced by strain-softening in rate-independent inelastic solids. *Computational Mechanics* 1993; **12**:277–296.
8. Oliver J. Modelling strong discontinuities in solid mechanics via strain softening constitutive equations. Part 2: Numerical simulation. *International Journal for Numerical Methods in Engineering* 1996; **39**(21):3601–3623.
9. Armero F, Garikipati K. An analysis of strong discontinuities in multiplicative finite strain plasticity and their relation with the numerical simulation of strain localization. *International Journal of Solids and Structures* 1996; **33**(20-22):2863–2885.
10. Wells GN, Sluys LJ. Application of embedded discontinuities for softening solids. *Engineering Fracture Mechanics* 2000; **65**(2–3):263–281.
11. Wells GN, Sluys LJ. Three-dimensional embedded discontinuity model for brittle fracture. *International Journal of Solids and Structures* 2001; **38**(5):897–913.
12. Simo JC, Rifai MS. A class of mixed assumed strain methods and the method of incompatible modes. *International Journal for Numerical Methods in Engineering* 1990; **29**(8):1595–1638.
13. Duarte CA, Oden JT. H-p clouds—an h-p meshless method. *Numerical Methods for Partial Differential Equations* 1996; **12**(6):673–705.
14. Melenk JM, Babuška I. The partition of unity finite element method: Basic theory and applications. *Computer Methods in Applied Mechanics and Engineering* 1996; **139**(1-4):289–314.
15. Fleming M, Chu YA, Moran B, Belytschko T. Enriched element-free Galerkin methods for crack tip fields. *International Journal for Numerical Methods in Engineering* 1997; **40**(8):1483–1504.
16. Belytschko T, Black T. Elastic crack growth in finite elements with minimal remeshing. *International Journal for Numerical Methods in Engineering* 1999; **45**(5):601–620.
17. Mões N, Dolbow J, Belytschko T. A finite element method for crack growth without remeshing. *International Journal for Numerical Methods in Engineering* 1999; **46**(1):131–150.
18. Belytschko T, Lu YY, Gu L. Element-free Galerkin methods. *International Journal for Numerical Methods in Engineering* 1994; **37**(2):229–256.
19. Oden JT, Duarte CAM, Zienkiewicz OC. A new cloud-based hp finite element method. *Computer Methods in Applied Mechanics and Engineering* 1998; **153**(1-2):117–126.
20. Babuška I, Melenk JM. The Partition of Unity Method. *International Journal for Numerical Methods in Engineering* 1997; **40**(4):727–758.
21. Hillerborg A, Modeer M, Petersson PE. Analysis of crack formation and crack growth in concrete by means of fracture mechanics and finite elements. *Cement and Concrete Research* 1976; **6**(6):773–782.
22. Rots JG. Computational modeling of concrete fracture. *Ph.D. Thesis*, Delft University of Technology, 1988.
23. Jirasek M. Embedded crack models for concrete fracture. In *EURO-C 1998 Computer Modelling of Concrete Structures*, de Borst R, Bićanić N, Mang H, Meschke G (eds). Balkema: Rotterdam, 1998; 291–300.
24. Schlangen E. Experimental and numerical analysis of fracture processes in concrete. *Ph.D. Thesis*, Delft University of Technology, 1993.
25. Peerlings RHJ, De Borst R, Brekelmans WAM, Geers MGD. Gradient-enhanced damage modelling of concrete fracture. *Mechanics of Cohesive-Frictional Materials* 1998; **3**(4):323–342.